

Supplementary Information for

A self-powered implantable and bioresorbable electrostimulation device for biofeedback bone fracture healing

Guang Yao^{a,b,e,1,2}, Lei Kang^{c,d,1}, Cuicui Li^{c,1}, Sihong Chen^b, Qian Wang^b, Junzhe Yang^c, Yin Long^{a,b}, Jun Li^a, Kangning Zhao^a, Weina Xu^a, Weibo Cai^{d,2}, Yuan Lin^{b,e,2}, Xudong Wang^{a,2}

^aDepartment of Materials Science and Engineering, University of Wisconsin-Madison, Madison, Wisconsin 53706, USA.

^bSchool of Materials and Energy, State Key Laboratory of Electronic Thin films and Integrated Devices, University of Electronic Science and Technology of China, Chengdu, Sichuan 610054, China.

^cDepartment of Nuclear Medicine, Peking University First Hospital, Beijing 100034, P. R. China.

^dDepartments of Radiology and Medical Physics, University of Wisconsin-Madison, Wisconsin 53705, USA.

^eSchool of Electronic Science and Engineering, the Center for Information in Medicine, University of Electronic Science and Technology of China, Chengdu, Sichuan 611731, China.

¹These authors contributed equally to this work.

²To whom correspondence may be addressed to X.W. (xudong.wang@wisc.edu) or G.Y. (gyao@uestc.edu.cn) or Y.L. (linyuan@uestc.edu.cn) or W.C. (wcai@uwhealth.org)

This PDF file includes:

Materials and Methods

Figure S1. The fabrication procedure of the FED.

Figure S2. Mechanical robustness of the FED.

Figure S3. Hydrophobicity of the PLGA encapsulation layer.

- Figure S4.** Schematic and optical images of Mg electrodes with different *L*.
- Figure S5.** Voltage output performance of the close-loop biofeedback system *in vivo*.
- Figure S6.** Long-term voltage output of FED *in vitro* and *in vivo*.
- Figure S7.** Tibia fracture modeling and FED implantation.
- Figure S8.** Hematology results of three groups during a 4-week implantation period.
- Figure S9.** Bone fracture healing analysis with and without intervention.
- Figure S10.** Bone density measurement in small areas.
- Figure S11.** Mechanical property of bones in different groups.
- Figure S12.** Schematic diagram of the relationship between OB, OC and growth factors.
- Figure S13.** IHC staining images of VEGF, FGF1, TGF- β and BMP2.
- Figure S14.** Immunofluorescence staining and expression intensity of growth factors.

Other supplementary materials for this manuscript include the following:

- Movie S1.** A stability test on an as-prepared FED for over 1200-cycle.
- Movie S2.** Voltage output at rat's normal activity.
- Movie S3.** Standardized midshaft fracture does not affect normal daily activity.

Materials and Methods

Device fabrication and encapsulation. The detailed fabrication process of the FED including a soft TENG and a pair of interdigitated electrodes is depicted in **Figure S1**. PLGA (lactide:glycolide=75:25, Sigma-Aldrich) was added to chloroform, followed by ultrasonic mixing and magnetic stirring to obtain a uniform PLGA dispersion solution (100 g/L). Inverse pyramid Si mold was fabricated according to reference²⁸. Specifically, $10\mu\text{m} \times 10\mu\text{m}$ SiO₂/Si arrays were obtained by lithography technique, and then the SiO₂ was etched by BOE (HF:NH₄F=6:1) and the arrayed Si was exposed to air. The remaining SiO₂ acts as the mask to etch the (001) Si arrays by the KOH and isopropyl alcohol mixed solution, and the inverse square pyramid arrays structured Si wafer mold was obtained. The PLGA solution was spin-coated on the Si wafer with the inverse square pyramid array structure at a spin-coating speed of 500~1000 r/min, and then dried in an oven at 60~100 °C for 18~24 h to remove the solvent. The PLGA films were peeled off as the functional P-PLGA layer. In addition, the PLGA solution was coated on a flat Si substrate followed by same treatment procedures as the encapsulation layer. Two Mg foils (30 μm) was adhered flatly on the heat release tape, and laser cutting technology was employed to prepare two Mg electrodes with an island-bridge structure and an interdigital structure as the top and bottom Mg electrodes, respectively. The upper and lower Mg electrodes were transferred to the PLGA encapsulation layers at a temperature of ~120 °C and thermoplastically fixed by a dot-matrix electric soldering iron at 200~300 °C. The lower Mg electrode/flat PLGA was combined with the P-PLGA layer to act as the bottom triboelectric layer and the upper one was defined as the top triboelectric layer. At last, the FED was thermoplastically encapsulated using a bilayer alignment mark. The overall FED device weight was approximately ~0.1 g.

Electrical characterization of the FED. The electrical performance of all FED devices were measure by a Keithley 6514 electrometer (USA, internal impedance is 200 TΩ). The voltage signals shown in **Figs. 2B-D, Figures S5, S6** and **Movie S1** were measured by a linear motor (LinMot-B01-37X166/160). The voltage signals in **Fig. 2F** (bottom) and **Figure S5B** were monitored *in vivo* when the rats with an implanted FED was anesthetized. Their knee joints were placed in flexion or extension state at 1 Hz to mimic the walking

action. The voltage signals in **Figure S5D** and **Movie S2** was monitored *in vivo* when the awake rats were at its normal activity.

Mechanical and EF simulation. The FEA of strain distribution was conducted using the ABAQUS software to evaluate the mechanical properties of island-bridge Mg electrode under different pressing height (**Fig. 1F** and **Figure S2**). The hexahedron element (C3D8R) model was used in the polydimethylsiloxane substrate, while the composite shell element (S4R) model was adopted in the Mg foil. An ideal elastic-plastic constitutive relation with a Young's modulus of 45 GPa, Poisson's ratio of 0.34, yield strain of 0.3% and fracture strain of 5% describe the mechanical behavior of the Mg electrodes. As for the elastomeric substrate, a typical hyper-elastic constitutive relation, the Mooney Rivlin law, was adopted to describe the mechanic properties (elastic modulus = 1 MPa, Poisson's ratio $\nu = 0.49$). The meshes were refined to ensure computational accuracy. For EF distributions simulation of the device, the Ansys Maxwell finite element solver was employed. In the simulation domain, the electrostatic solution type was used. The model of salt water was created with the permittivity of 81 to simulate tissues and body fluids, while the Mg foil was assigned with the conductivity of $\sigma = 2.25 \times 10^7$ S/m (**Figs. 2G** and **H**).

Cell immunofluorescence staining. The cytoskeleton and nucleus were stained with Texas red-X phalloidin (591/608 nm) and blue fluorescent Hoechst (352/461 nm) (Thermo Fisher Scientific), respectively. In brief, the samples were first fixed with 2-4% formaldehyde for 15 min and rinsed three times with pre-warmed PBS. The samples were then stained with texas red-X phalloidin (100 nM) and Hoechst (50 nM) for 30 minutes at 37 °C. After staining, cells were rinsed with pre-warmed buffer for 3 times and imaged using a Nikon A1RS confocal microscope.

MTT assay. After 3T3 cells were cultured on the packaging film on 24-well plates, assay of 3-{4,5-dimethylthiazol-2-thiazolyl}-2,5-diphenyl-2H-tetrazolium bromide (MTT, ThermoFisher scientific) was performed to evaluate cell proliferation. 100 μ L of MTT solution was added to each well (n=3) and incubated at 37 °C in a humidified atmosphere with 5% CO₂ for up to 3 days. At each time point, the medium was removed and dimethyl sulfoxide (500 μ L/well) was added to dissolve the precipitated fomazan. The optical density was measured using a Synergy H1 microplate spectrophotometer (BioTek) at a wavelength of 490 nm.

Animals and diets. Six-week-old female Sprague-Dawley (SD) rats were housed in separated cages at a temperature-controlled room (22 °C) with a 12-h light/dark cycle with free access to water and Purina PMI-certified rodent chow 5002 (LabDiet, MO, USA). All animal experiments were performed following the standard protocol approved by the University of Wisconsin Institutional Animal Care and Use Committee, and the Institutional Animal Care and Use Committee in Peking University First Hospital (201822).

Fracture modeling and device implantation. The production of a standard closed tibia fracture was accomplished by 3-point bending apparatus³⁶. First, rat anesthesia was induced by inhalation of 2-5% isoflurane and maintained with 2% isoflurane. Under the condition of anesthesia, rats were fixed on supine position. The right leg was shaved and scrubbed with iodine in preparation for surgery. After a skin incision (~1 cm) was made, the tibia plateau was exposed and drilled using an electrical driller. A steel needle with a diameter of 0.8 mm was inserted through the hole into bone marrow cavity for the purpose of internal fixation. Then the tibia of supine rat was positioned and fixed over the support anvils of the 3-point bending apparatus with a guillotine blade snug and an intermediate tibia diaphysis. The ramming system with 500 g weight dropped from a height of 35 cm can produce a standard closed fracture with a transverse configuration. For group I, skin incision around the right leg was made for about 3-5 cm. The FED was implanted in the rats with the interdigitated Mg dressing electrodes wrapped around the fracture foci and the TENG fixed at the site between knee joint and hip to make sure that it worked normally when body moved (n=7). To prevent the device from moving and falling off, the FED was stitched to the muscle by needle fixation with degradable suture. For group S, a deactivated FED device was implanted similarly (n=7). Group F was created followed all the surgical process without the implantation of FED (n=7). Finally, the incision was sutured layer by layer followed with sterilization. The implantation procedure was shown step-by-step, and rats were permitted full weight-bearing on awakening from anesthesia (**Figure S7**).

H&E staining of skin and vital organs. Skin at implanted site and some vital organs including heart, liver, spleen, kidney, and lung were collected from rats for H&E staining after euthanasia at 1, 2, 4 and 6 week post implantation. Tissues were fixed with 4% formaldehyde and slices were prepared at 3 µm for H&E staining.

X-ray radiograph scan. X-ray scanning was performed preoperative, postoperative weekly (1-6 weeks). In brief, rats were placed in the prone position after anesthesia and scanned by an ultrafocus60 X-ray scanner (Faxitron, USA). X-ray radiographs were taken to monitor the formation process of external callus and internal callus, and to evaluate the process of fracture healing.

Bone mineral density. Bone density was measured using a Discovery Wi bone densitometer (Hologic, USA) after the terminal time point of X-ray scanning. After right legs were collected, the internal needles were removed. The bone density was measured at the region of bone fracture in tibia following the manufacturer's instructions for small animal study.

Bending mechanical measurement. A universal testing machine (Hengyi, China) was employed to measure the biomechanical properties of the right tibia by a 3-point bending test. Both ends of the tibia was positioned and fixed on a 1.5 cm-distant support platform, and the force application component was snug with the fracture site of the tibia diaphysis. The bending force was applied at a constant deformation rate of 1 mm/min until fracture to obtain the maximum load and bending flexural stress at failure (**Fig. 4C** and **Figure S11**).

Immunohistochemistry properties of bone. The collected rat tibias were fixed in 10% formaldehyde solution for 48 hours, decalcified with 5% nitric acid, and embedded in paraffin following dehydration and washing. Sequential parts were cut parallel to the region of bone fracture using a microtome for each specimen. Immunohistochemical (IHC) staining was performed to evaluate the level of VEGF, FGF1, TGF- β and BMP2. The procedure of IHC of formalin-fixed paraffin-embedded bone samples (**Fig. 5B** and **Figure S13**). Mouse anti-VEGF (NB100-664, Novus), rabbit anti-FGF1 (ab9588, abcam), rabbit TGF- β (NBP1-80289, Novus), and rabbit anti-BMP2 (ab14933, abcam) antibodies were used at dilutions of 1:100, 1:100, 1:200, and 1:200, respectively as the primary antibodies, respectively.

Immunofluorescence staining of the bone. Frozen bone samples of 10 μ m thickness were fixed with cold acetone for 5 min, washed with cold PBS and then blocked with 2% donkey serum for 1 h at room temperature. Slices were then incubated with Rabbit-anti-rat/mouse VEGF antibody, TGF- β antibody and BMP antibody (Thermo Fisher) at 4 degrees Celsius overnight. After washing with cold PBS for three times, slices were then stained with

Alaxa488-labeled Donkey-anti-Rabbit antibody (Thermo Fisher) for 1 h. After three rounds of washing with cold PBS, all slides were mounted with hard-set mounting medium with DAPI (Santa Cruz Biotechnology) and covered with cover slides for imaging using a Nikon A1R confocal microscope (Nikon instruments) (**Fig. 5C** and **Figure S14**).

Statistical analysis. Statistical analysis was performed by two-tailed unpaired Student's t tests for bone mineral density and 3-point bending flexural stress (**Figs. 4B** and **C**), IHC score of the various growth factors and OB counts (**Figs. 5D-F**). In box plots, dot is the mean, center line is the median, box limits are the lower quartile (Q1) and upper quartile (Q3), and whiskers are the most extreme data points that are no more than $1.5 \times (Q3 - Q1)$ from the box limits. n.s, ** and *** represent non-significant ($P > 0.05$), $P < 0.01$ and $P < 0.001$, respectively. In general, p value less than 0.05 indicates a significant difference.

Figure S1

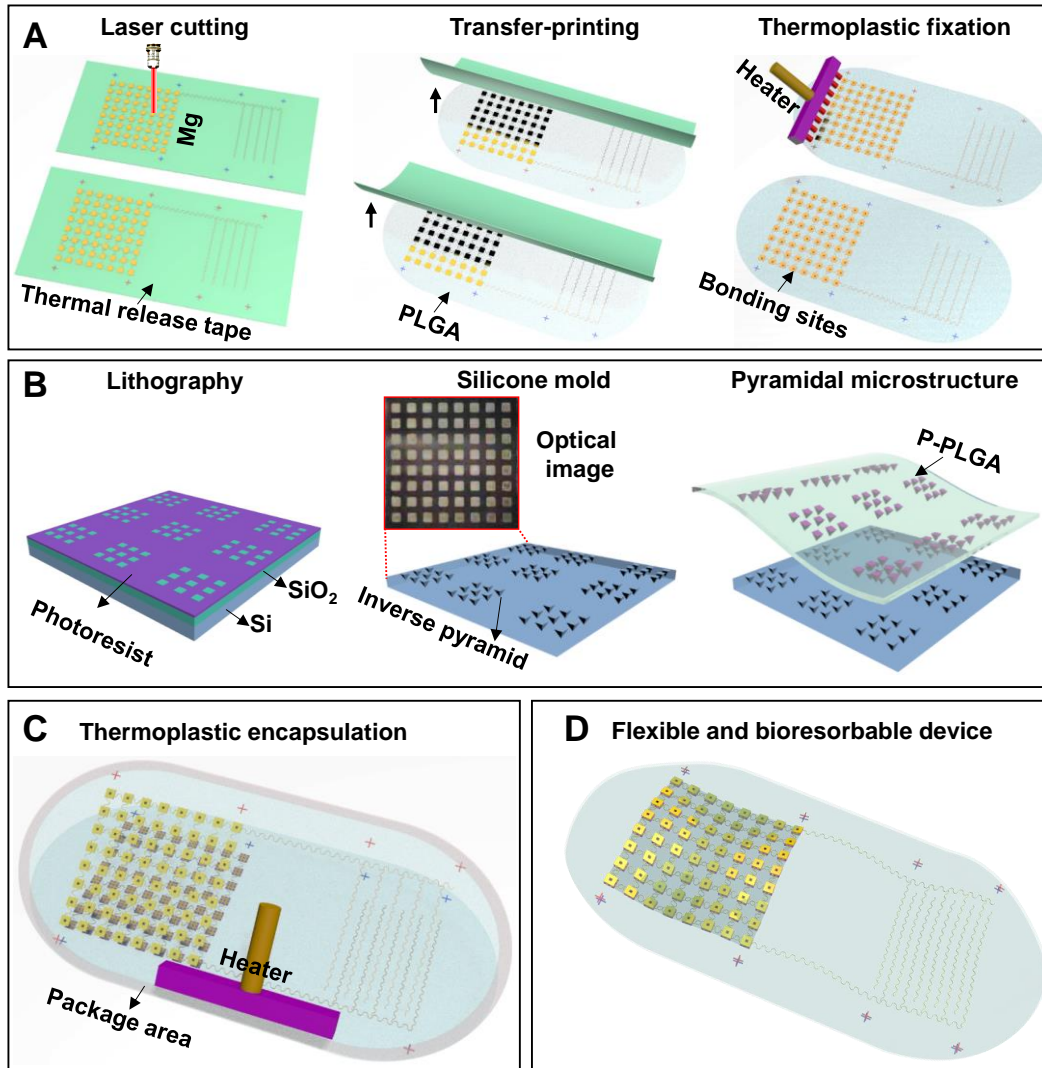


Figure S1. The fabrication procedure of the FED. (A) Mg foils adhered on the heat release tape were patterned to island-bridge and an interdigital structure by laser cutting technology. The top and bottom Mg electrodes were transferred and printed on PLGA substrates at 120 °C, and then thermoplastically fixed on the PLGA substrates by a dot-matrix electric soldering iron. **(B)** Inverse square pyramid arrays structured Si wafer mold was fabricated by lithography and wet-etching techniques, and the P-PLGA substrate was peeled from the Si mold following solution spin coating and drying. **(C)** The FED was thermoplastically encapsulated according to bilayer alignment marks with the P-PLGA inserted in two Mg electrodes. **(D)** Schematic of the flexible and biodegradable FED.

Figure S2

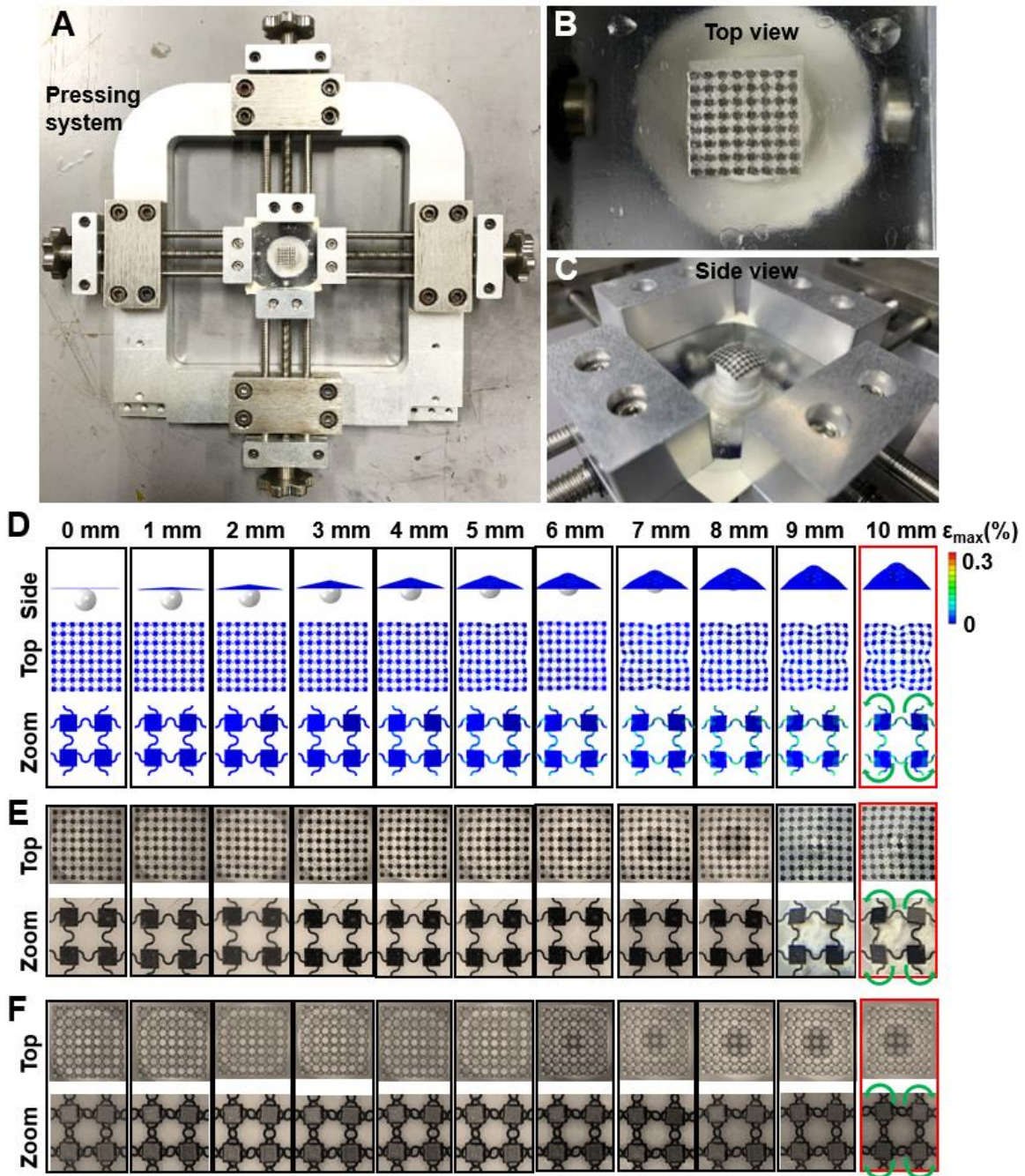


Figure S2. Mechanical robustness of the FED. (A) Optical image of the overall pressing system. (B) Top view and (C) Side view of the TENG pressed with a spherical plastic ball with a radius of 4 mm. (D) FEA and experimental results of the island-bridge Mg electrode under a series of pressing heights both demonstrate that the strain ($< 0.3\%$) was primarily distributed on the serpentine line. (E) Corresponding height experimental results of the

island-bridge Mg electrode. Both the FEA results and corresponding height experimental results have a similar deformation trend, where the serpentine line was stretched and adjacent island-bridge units rotated in opposite directions to release stress. (F) The TENG can be repeatedly pressed up to 10 mm without damage.

Figure S3

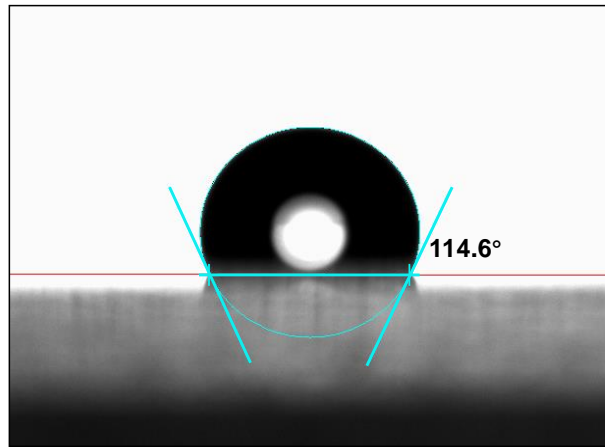


Figure S3. Hydrophobicity of the PLGA encapsulation layer. The contact angle of the PLGA encapsulation layer was 114.6° , confirming its hydrophobic surface. This property is desired for a long-term operation in biological environment.

Figure S4

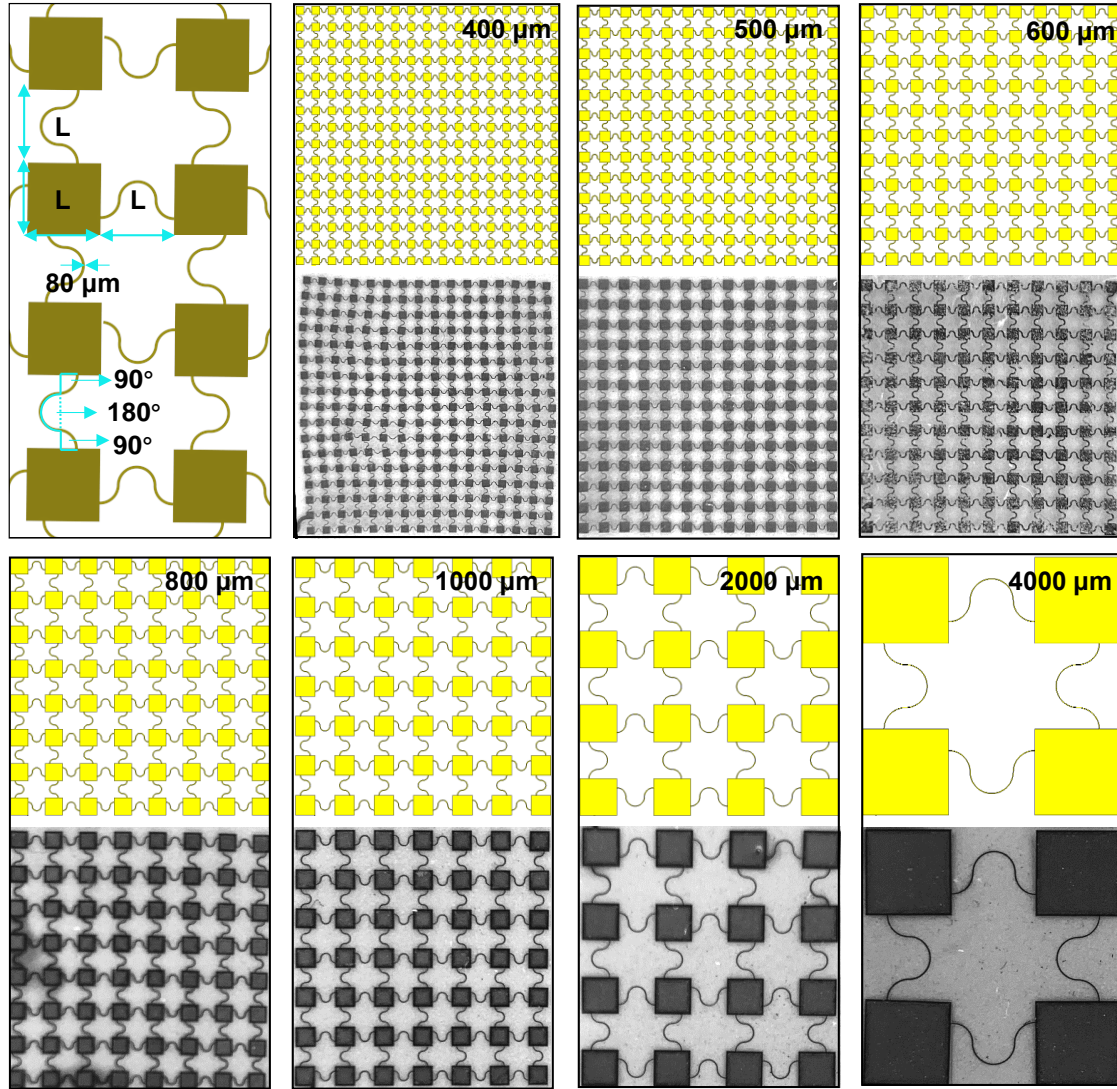


Figure S4. Schematic and optical images of Mg electrodes with different L . The yellow and black pictures represent the schematic and physical images, respectively. The lengths of Mg electrode islands were equal to their spacing. The serpentine connecting line consisted of a semicircle and two quarter circles, and the arc radius and width of the serpentine line were $L/4$ and $80 \mu\text{m}$, respectively.

Figure S5

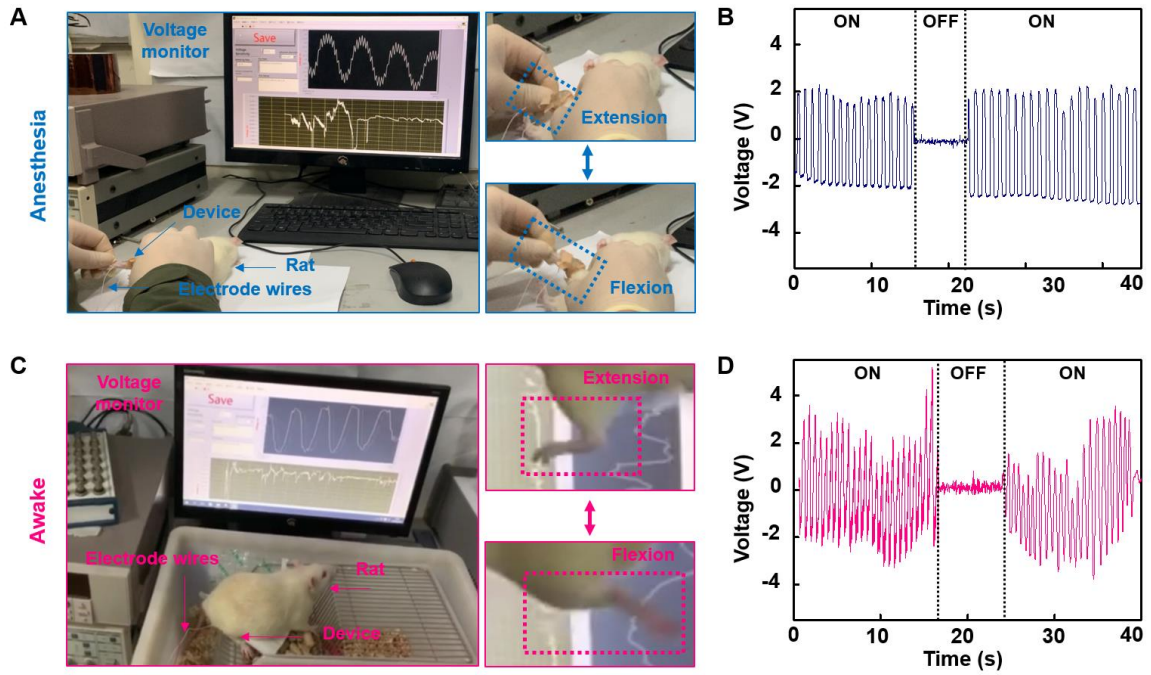


Figure S5. Voltage output performance of the closed-loop biofeedback system in vivo. (A) Voltage measurement of the FED under the anesthesia state of the rat. (B) Voltage output under the anesthesia state. (C) Voltage measurement of the FED under the awake state of the rat. (D) Voltage output under the awake state.

Figure S6

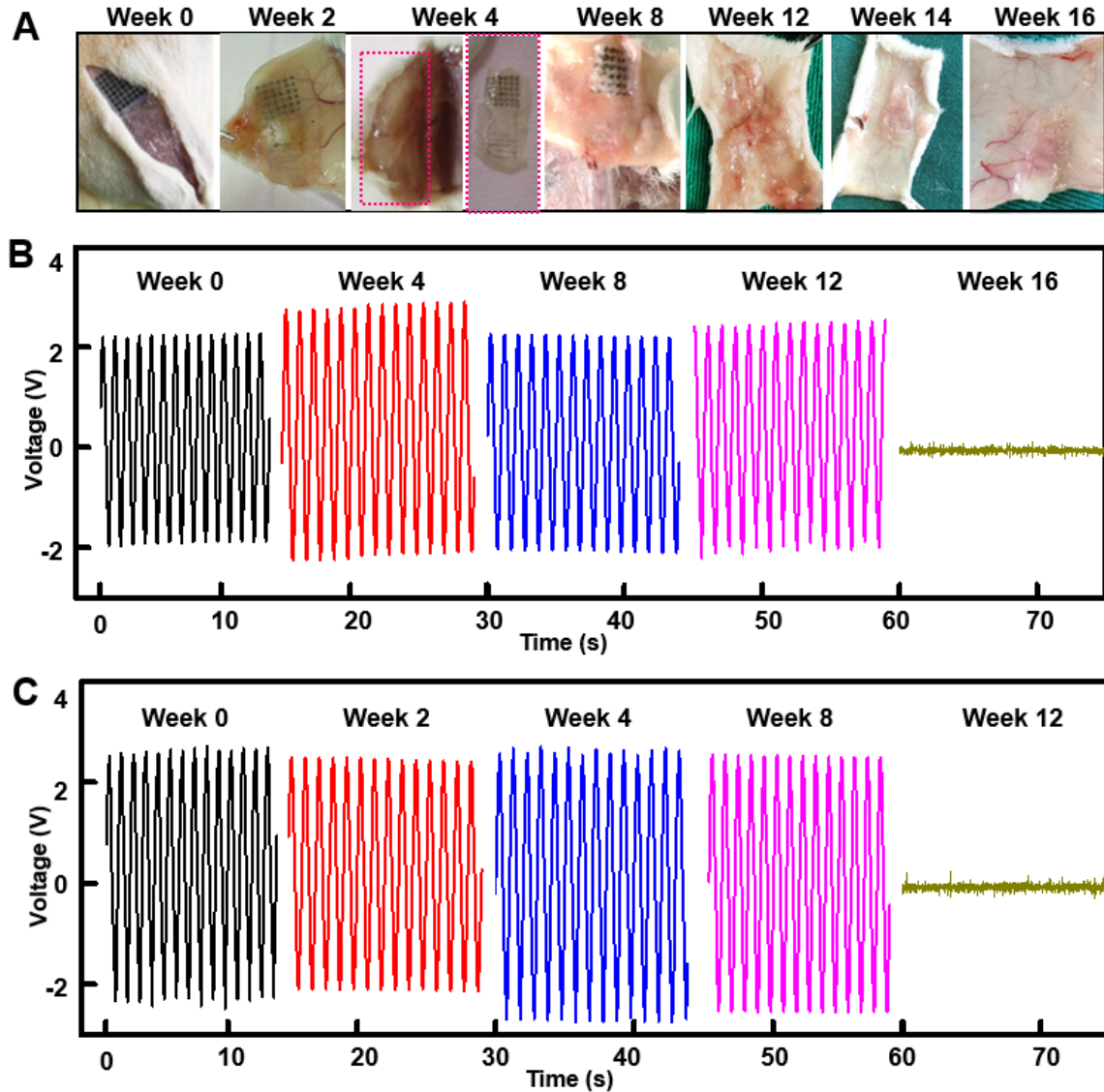


Figure S6. Long-term voltage output of FED in vitro and in vivo. (A) The *in vivo* biodegradation and bioresorption process of the small-sized FED. The FED was gradually surrounded and covered by fibrous tissue due to its good biocompatibility, the coated fibrous tissue was cleaned to clearly demonstrate the degradation and absorption state of the FED. (B) The 16-week output performance of the FED in a PBS solution at 37 °C. (C) Voltage outputs at different time points from the harvested implanted FEDs.

Figure S7



Figure S7. Tibia fracture modeling and FED implantation. (A) Surgical procedure including needle fixation, 3-point bending, FED fixation and device implantation. **(B)** Rats can bear weight after awakening from anesthesia, indicating that the fracture model does not affect their normal life.

Figure S8

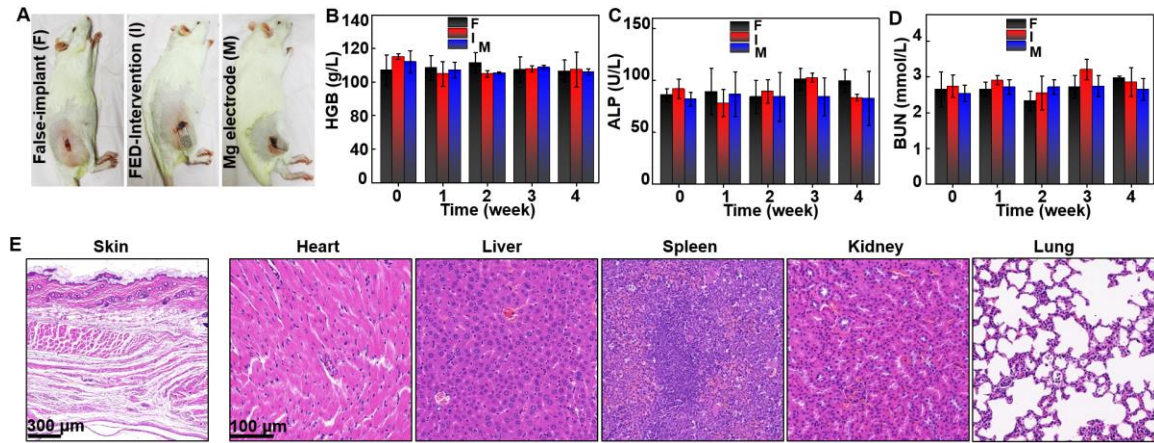


Figure S8. Hematology results of three groups during a 4-week implantation period.

(A) Implantation images for the intervention (I), Mg-implant (M) and false-implant (F) groups. (B) Hematopoietic function-related hemoglobin (HGB) levels. (C) Hepatological function-related alkaline phosphatase (ALP) levels. (D) Renal function-related blood urea nitrogen (BUN) levels. (E) H&E stains of skin at the implantation site and vital organs (heart, liver, spleen, kidney and lung) at week 4 post implantation of the separate Mg electrode. All data in (B–D) are presented as mean \pm s.d (n = 3).

Figure S9

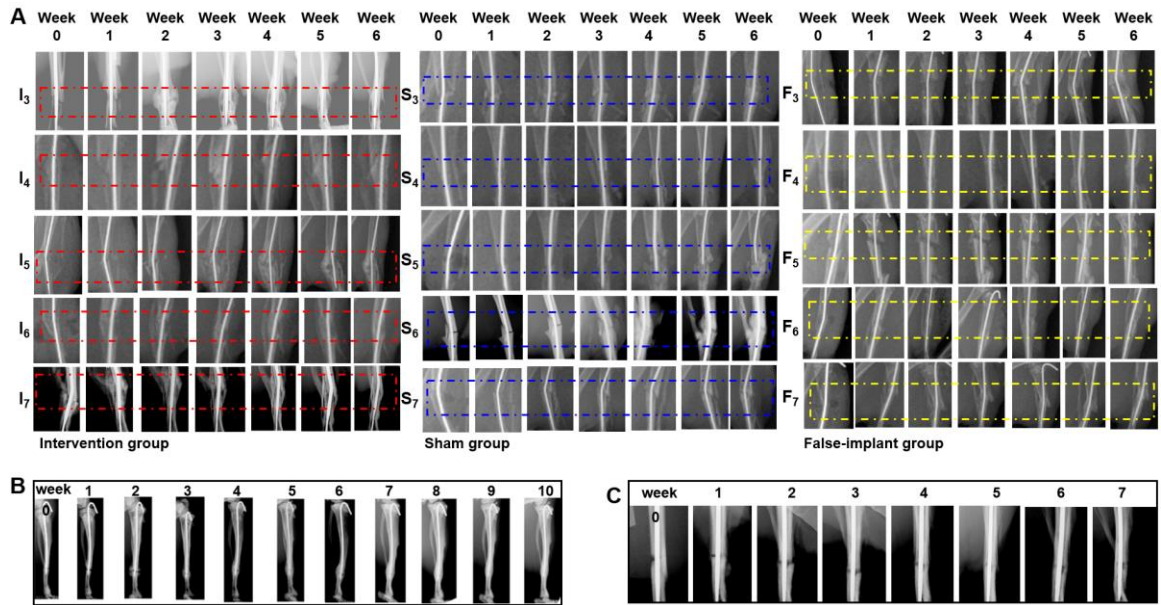


Figure S9. Bone fracture healing analysis with and without intervention. (A) Serial X-ray radiographs over time of the I, S and F group, respectively. **(B)** The fracture line did not completely disappear at the week 10 with ES intervention. **(C)** A rat without ES intervention did not form an external or internal callus during the 7-week experiment, which represents the symptoms of nonunion.

Figure S10

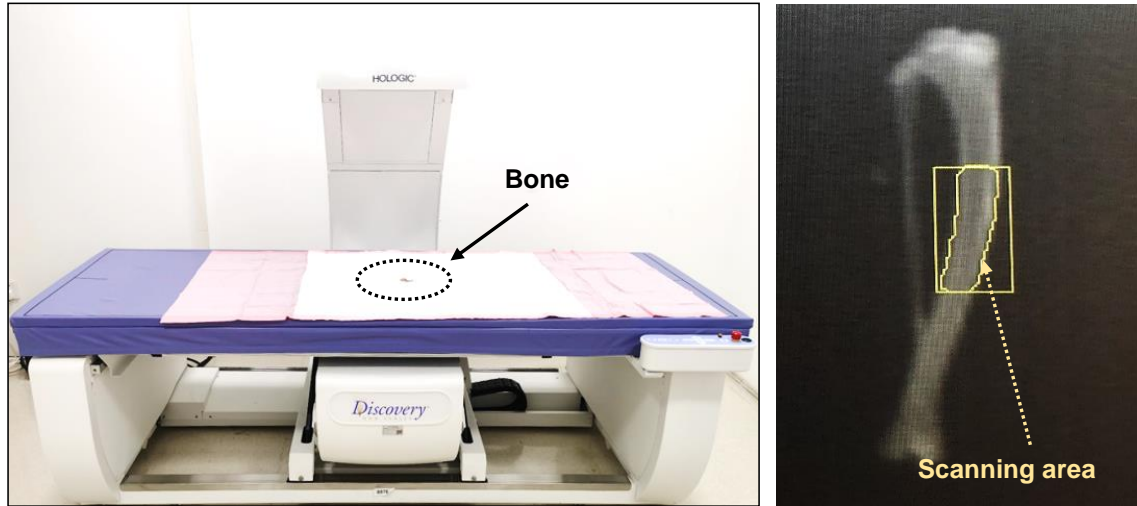


Figure S10. A Discovery Wi bone densitometer for bone density measurement in small areas.

Figure S11

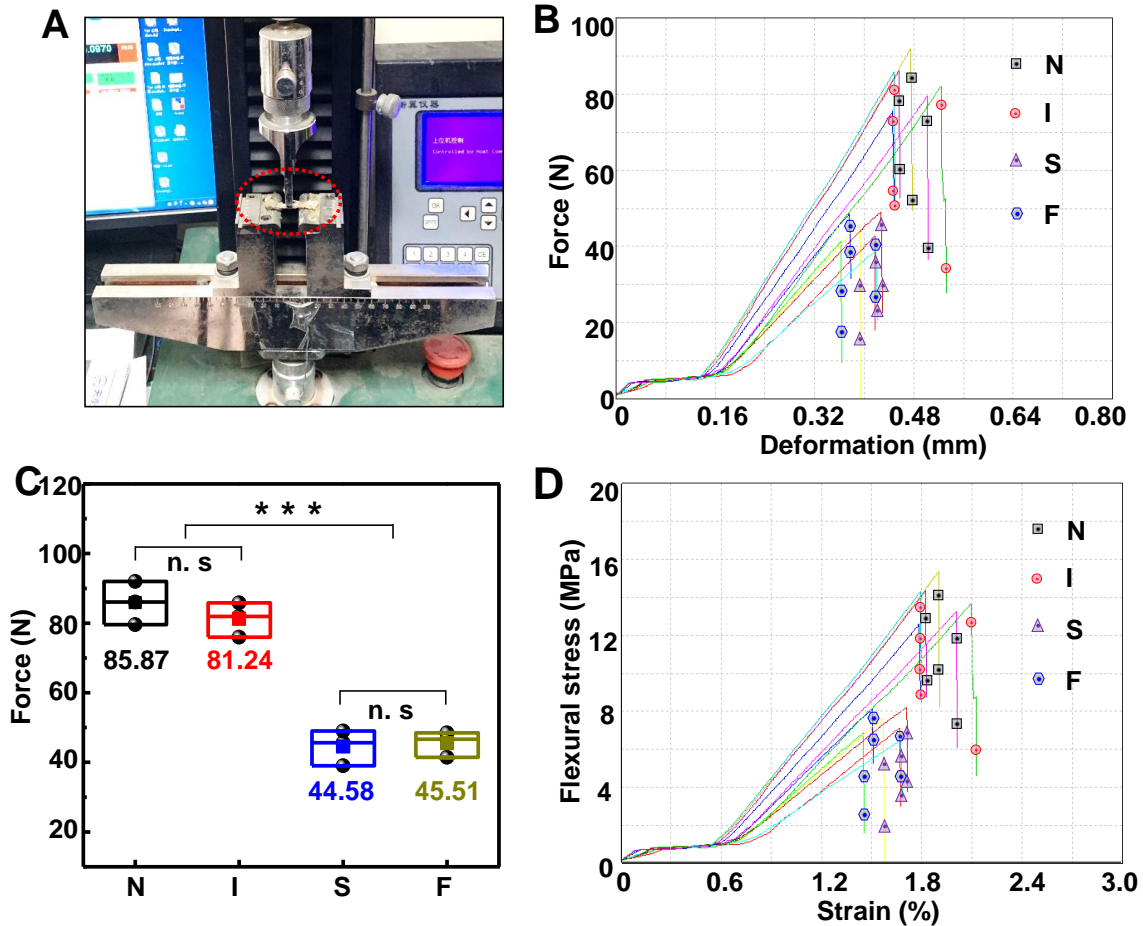


Figure S11. Mechanical property of bones in different groups. (A) Optical image of a universal testing machine for 3-point bending test, and the bone was positioned and fixed on a 1.5 cm-distant support platform (red dotted circle). (B) Load versus deformation curves for bones in different groups. (C) A statistically significant ~80% improvement of maximum load was observed in group I (81.24 N) over the control groups (44.58 N and 45.51 N for group S and F, respectively). (D) Flexural stress versus deformation curves for bones in different groups.

Figure S12

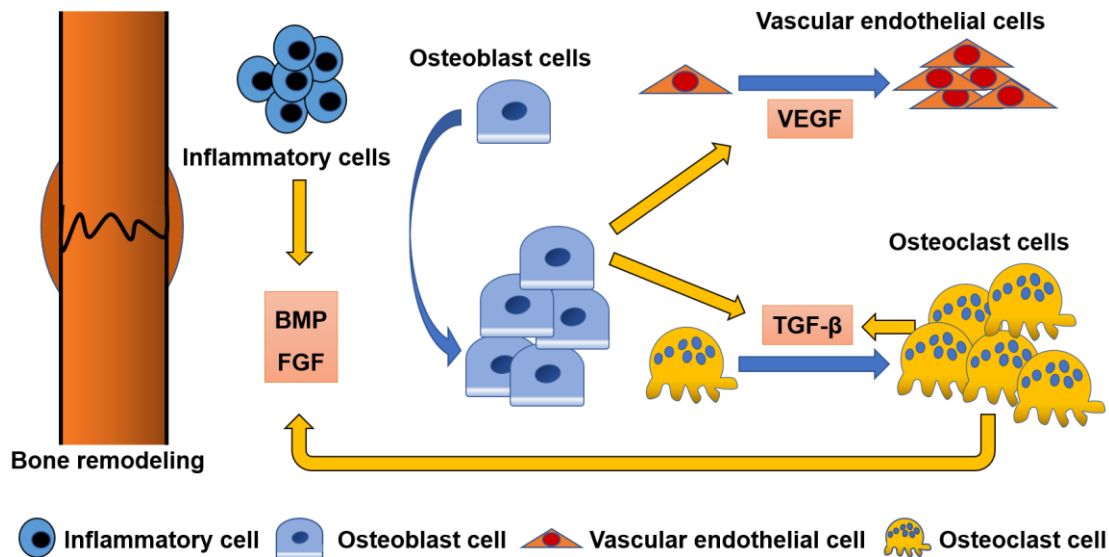


Figure S12. Schematic diagram showing the relationship between OB, OC and growth factors. After the phase of inflammation, the inflammatory cells secrete some growth factors such as FGF1 and BMP2, which improve the proliferation and differentiation of OBs to build bone tissues in the bone formation phase. Meanwhile, OBs induce and enhance the secretion of TGF- β and VEGF. VEGF can promote the vascularization process to provide more blood supply. TGF- β , BMPs, and FGFs induce the formation of OCs via direct and/or indirect mechanisms such as receptor activator of nuclear factor- κ B ligand (OC differentiation factor). The increase of the number of OCs is an important sign of bone entering the remodeling phase along with the replacement of large fracture spongy callus by compact bone. Meanwhile, many factors including TGF- β , BMPs, FGFs, and IGFs can be released from bone matrix during the bone resorption by OCs, and these factors improve the genesis of OBs and OCs in the fracture repairing process.

Figure S13

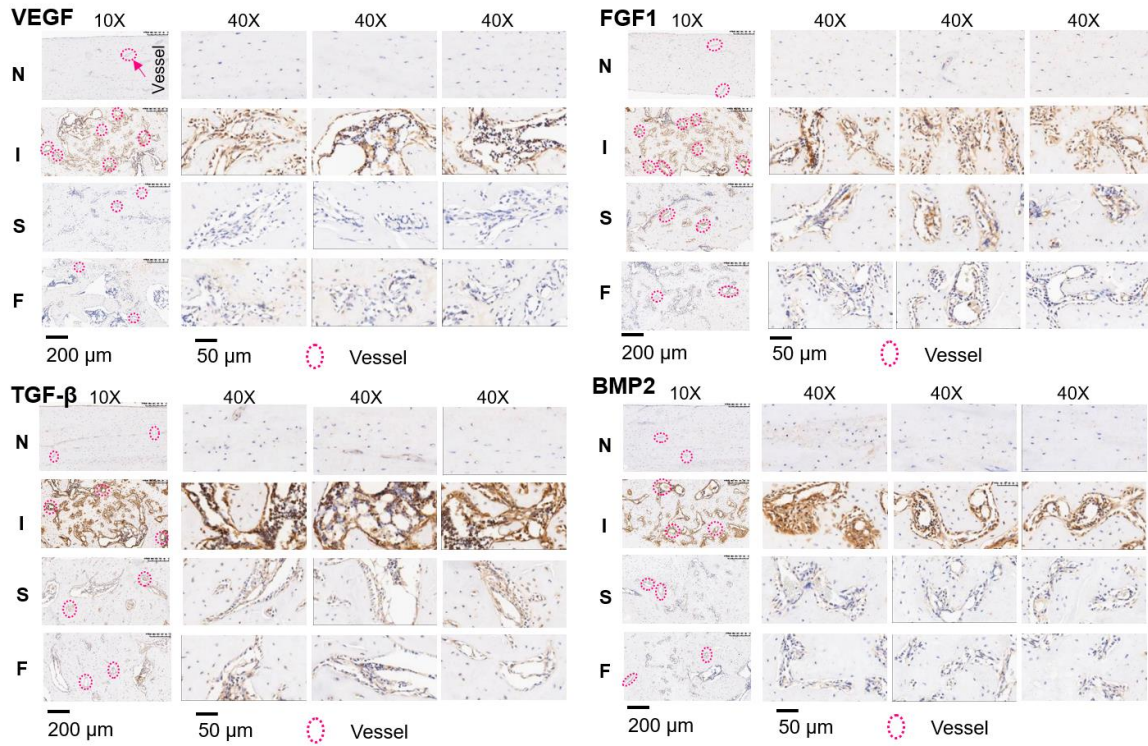


Figure S13. IHC staining images of VEGF, FGF1, TGF-β and BMP2.

Figure S14

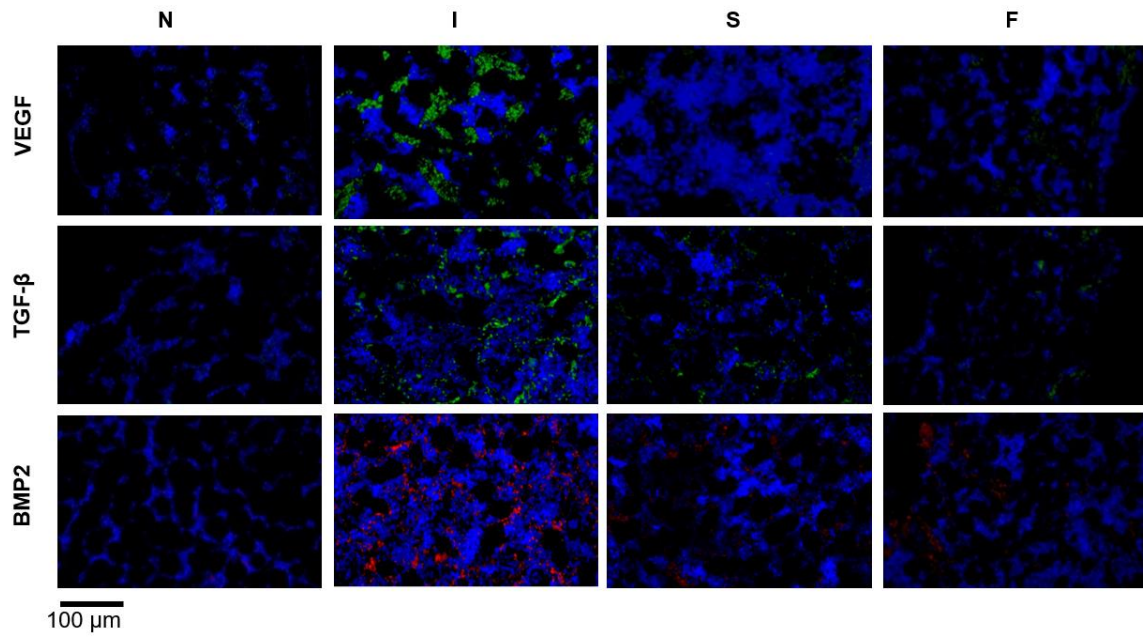


Figure S14. Immunofluorescence staining and expression intensity of growth factors.